Journal of
Synchrotron Radiation

ISSN 0909-0495

Received 26 March 2008
Accepted 21 April 2008

A high-spatial-resolution three-dimensional detector array for 30–200 keV X-rays based on structured scintillators

U. L. Olsen,* S. Schmidt and H. F. Poulsen

Center for Fundamental Research: Metal Structures in Four Dimensions, Risø National Laboratory, DK-4000 Roskilde, Denmark. E-mail: ulrik.lund.olsen@risoe.dk

A three-dimensional X-ray detector for imaging 30–200 keV photons is described. It comprises a set of semi-transparent structured scintillators, where each scintillator is a regular array of waveguides in silicon, and with pores filled with CsI. The performance of the detector is described theoretically and explored in detail through simulations. Based on available hardware, a spatial resolution of 1 μm is obtainable. The resolution of a single screen is shown to be determined only by the pitch, at least up to 100 keV. In comparison with conventional homogeneous screens, an improvement in efficiency by a factor of 5–15 is obtainable. The cross-talk between screens in the three-dimensional detector is shown to be negligible. The three-dimensional concept enables ray-tracing and super-resolution algorithms to be applied.

Keywords: scintillator; detector; imaging; hard X-rays; simulation.

1. Introduction

In recent years more synchrotrons have been and are being built, and as the X-ray community gains access to synchrotron radiation they are progressing to harder X-rays to better investigate larger bulk samples. At the same time the need to resolve details at a micrometer or even submicrometer level continuously increases, bringing forth the need for high-spatial-resolution X-ray imaging at energies between 30 and 200 keV (Banhart, 2008). Additionally, the need for dynamic studies demands high-efficiency detectors to obtain fast time-resolved data (Baruchel *et al.*, 2006).

Presently, for such purposes detectors comprising a homogeneous scintillator optically linked to a CCD are used almost exclusively at synchrotron facilities (Koch *et al.*, 1998). Unfortunately this design has two serious drawbacks. Firstly, the visible photons are emitted in a Lambert-like distribution within the scintillator, and hence the spatial resolution of the detector is limited by the thickness of the scintillating screen, since the light will be out of focus for all but one narrow depth. Secondly, for support purposes, scintillators are typically mounted on thicker substrates, and Compton scattering and fluorescence in the substrates then give rise to tails in the point spread function (PSF).

As an example, a typical scintillator used at the European Synchrotron Radiation Facility (ESRF) is a 6 μm-thick crystal of YAG, LAG or YAP doped with cerium on a 100 μm-thick substrate. This is used in hard X-ray tomographic experiments with a resolution of 2 μm, but in the white beam used for these studies the efficiency is only approximately 1.1% (Martin & Koch, 2006; Di Michiel *et al.*, 2005). The strong coupling between spatial resolution and efficiency reduces options for time-resolved studies. This is true for tomographic studies, but the problem has been accentuated by the recent introduction of three-dimensional X-ray diffraction microscopy (3DXRD) (Poulsen, 2004), which is based on diffraction.

These disadvantages are well known and several alternative detector designs have been suggested in the literature. One direction of research is towards semiconductor detectors with three-dimensional anodes (Piemonte *et al.*, 2005), but the demand of space to make the necessary contact between columns and readout electronics sets a lower limit for the resolution at about 10 μm. A second direction of research is towards the manufacturing of scintillation screens confining and guiding the secondary emitted photons through the screen. This approach was described by Deckman *et al.* (1989) and by Bigler & Polack (1985), but their designs were hampered by very short pores and the use of a liquid scintillator with low efficiency, respectively.

The fabrication of a structured scintillator is reported in two recent papers (Badel, 2005; Olsen, 2007), showing the feasibility of manufacturing two-dimensional pore arrays with a distance between pore centers (pitch) of 40 and 4 μm, respectively. The waveguides comprise high-aspect-ratio pores in silicon with a wall coating of thermally annealed SiO_2 and a filling of the dense fluorescent material CsI. The pores are

obtained through electrochemical etching (Lehmann, 2002), a technique capable of producing deep arrays of submicrometer pores (Lehmann & Gruning, 1997).

In the first part of this paper we study the performance (spatial resolution and efficiency) of this novel type of scintillator by means of Monte Carlo (MC) simulations. Results are compared with the work of Koch *et al.* (1998) on unstructured scintillators. The results can be used to direct the on-going research and development towards the optimal fabrication parameters.

In the second part of the paper we explore the concept of a three-dimensional detector. By stacking a set of identical semi-transparent detectors, each comprising a structured scintillator screen, images are taken in parallel increasing the overall efficiency of the detector. Furthermore, the multiple simultaneous images enable the use of super-resolution algorithms (Park *et al.*, 2003) to further increase the detail level in the image. The three-dimensional detector can also be foreseen to be used in connection with divergent beams, in particular for non-destructive mapping of grain shapes and orientation fields by 3DXRD. 3DXRD involves acquiring diffraction images of different sample-to-detector distances to accurately ray-trace the origin of grains (Poulsen *et al.*, 2001).

However, the scintillators placed in the beam path will generate fluorescence and scattered photons and as such give rise to additional noise in the neighboring screens. A set-up using three screens placed behind each other has been simulated to evaluate the magnitude of these effects, and thereby assess the prospect of such a 'three-dimensional detector' principle.

2. Detector principle

The scintillator presented here is an adaptation of a design used by Badel *et al.* (2002). In an effort to achieve high efficiency while maintaining good resolution, the scintillator comprises a matrix of waveguides with scintillating cores. In Fig. 1 the principle of the waveguiding scintillator is shown. Pores are etched into a wafer of silicon which is opaque to visible light and separates the individual pores from cross-talk. A thermally grown surface layer of silicon dioxide on the pore walls acts as a waveguide cladding with a refractive index of 1.45 and the pores are filled with a high-refractive-index scintillator material, enabling total internal reflection in the pores.

Filling is achieved by melting the scintillating material into the pores. Si and SiO_2 have melting points around 1673 K and the scintillator is thus restricted to a material that will liquify well below this temperature. CsI doped with thallium has a melting temperature of 894 K, a rather high density of 4.15 g cm^{-3} and the light yield is among the highest of conventional scintillators with 60 photons per keV (Holl *et al.*, 1988). Compared with a few regularly used scintillating crystals like YAG, BGO and LAG, the absorption cross section of CsI matches or exceeds the alternatives between 40 and 80 keV.

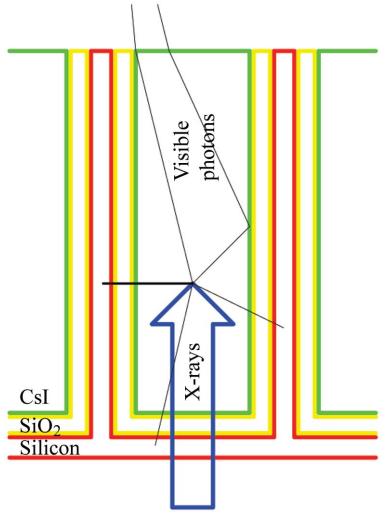

Figure 1
Schematic of a structured scintillator showing an absorption event and the internal reflection of secondary emitted photons.

SiO_2 comprises the cladding in the waveguide. The cladding thickness should be thick enough compared with the wavelength of the guided light to give effective internal reflection, and thin enough that it does not comprise too much of the screen area, thus lowering the efficiency. From the simulations shown in Fig. 2, it is found that a SiO_2 layer of 100 nm to 150 nm on a pure silicon wall of 150 nm to 50 nm is sufficient to have less than 1% of the wave intensity extend past the neighboring boundary. This means that absorption in the silicon and cross-talk is limited, and in the MC simulations of the detector response in §4 both effects are neglected.

The pores are filled with the scintillating material CsI with a refractive index of 1.73. Internal reflection in the pores occurs at angles above 56° from normal incidence. Assuming an isotropic emission of visible photons and neglecting reflections from angles below 56°, 8.5% of the emitted photons will be reflected forward. However, since the numerical aperture of

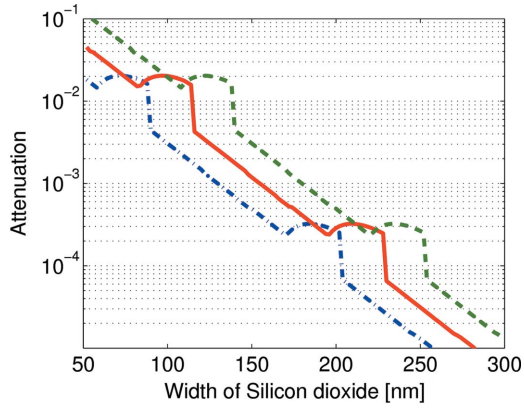

Figure 2
Result from electromagnetic wave simulation for waveguiding structures. The graph shows the amount of the total wave that extends past the middle of the wall. The remaining wall consists of unannealed silicon, and the three curves represent different thicknesses of the pure silicon; the dash-dotted line represents 150 nm, the solid line 100 nm and the dashed line 50 nm.

a subsequent lens only accepts incoming photons at certain angles, the internal reflection mechanism is only limiting efficiency if the numerical aperture of the lens is above 0.5, otherwise the collecting angle of the lens is the limiting factor.

Emission of visible photons occurs when X-rays are absorbed in the scintillating material. The absorption cross section of silicon and silicon dioxide are orders of magnitude smaller than the cross section of CsI, and even with a 400 µm-thick base of unstructured silicon the energy absorption in the silicon base and walls for screens with typical dimensions of the scintillating material and the silicon structure does not exceed 12% of the total absorbed energy of 50 keV X-rays.

2.1. Efficiency *versus* numerical aperture

The numerical aperture (NA) of the lens and the thickness of the scintillator z plays a vital role for the spatial resolution of the detector. The image that is generated on the CCD is a convolution of the image generated in the focal plane of the scintillator and the images at every other distance δz_n from this plane. Images generated in planes with a large δz will be out of focus and deteriorate the final image. From the work of Koch and co-workers (Koch *et al.*, 1998), the following correlation between NA, thickness z, resolution $R_{90\mathrm{W}}$ and efficiency η has been found,

$$R_{90\mathrm{W}} = \left[(pz)^2 + (pq/\mathrm{NA})^2\right]^{1/2}, \tag{1}$$

$$\eta = [1 - \exp(\sigma z \rho)]\frac{1}{2\pi}[1 - \cos(\mathrm{NA}/n)], \tag{2}$$

where p and q are empirically found constants, n is the refractive index of the media between the sample and lens, and ρ and σ are the density and the absorption cross section of the scintillator, respectively. From this equation the optimal parameters for the thickness and NA can be expressed,

$$z_{\mathrm{opt}} = \frac{1}{2pq}R^2 \tag{3}$$

and

$$\mathrm{NA}_{\mathrm{opt}} = 2^{1/2}p\frac{1}{R}. \tag{4}$$

For a low NA the resolution is diffraction limited and at a higher NA the shallower depth of focus will deteriorate the resolution; hence, for a given resolution, equation (3) gives the optimal NA to be used for the lens that allows the highest z. A thick scintillator gives good absorption of X-rays and thus high efficiency, but for a good signal-to-noise ratio the generated photons from the absorption processes should also be effectively collected for good photon efficiency, and these equations illustrate the advantages of the structured scintillator in terms of photon efficiency. Highly magnifying lenses typically have large apertures. Conventional scintillators rely on a lens with a low NA and a low magnification and the CCD should thus have small pixels. With the structured scintillator, only one focal plane exists and any lens gives sharp images. This allows the use of more efficient CCDs with larger pixels, and the high NA of the lens gathers more light, hence increasing the overall photon efficiency. Since resolution and lens parameters are decoupled, a structured scintillator can be used without a lens directly on a photodiode for further collecting power.

2.2. Three-dimensional detector

The multiple scintillators in the three-dimensional detector are placed on the beam path with tilted mirrors to reflect the visible light through a lens onto a camera. The distance between scintillators depends on the configuration of the mirrors. Two possible configurations have been suggested, as shown in Fig. 3. The first has a large distance between the scintillators to accommodate mirrors; the second has the scintillators close to each other but with the scintillators emitting light of different wavelengths, and laser-line mirrors are used to separate the signals from each detector. The first layout is suitable for structured scintillators, while the second layout makes it possible to place the scintillators close to each other. The final design of an actual detector is still on the

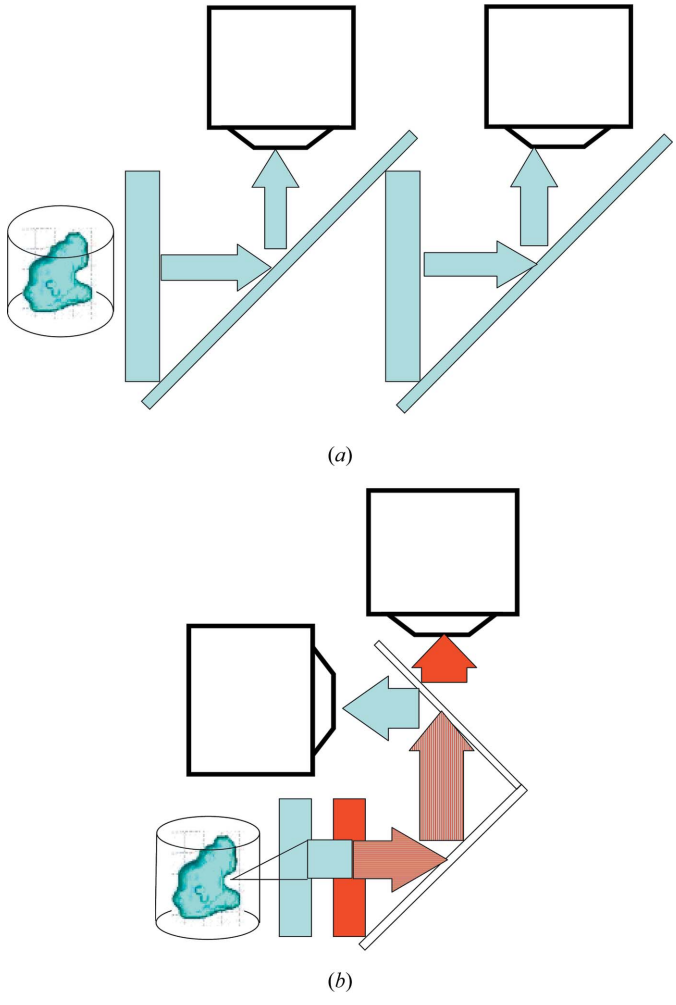

Figure 3
Two possible configurations of a three-dimensional detector, here shown with two scintillators. (*a*) Layout with mirrors between the scintillators. (*b*) Layout with scintillators emitting light at different wavelengths; the laser-line mirror separates the light from different scintillators.

drawing board, but scattering from one scintillator that is absorbed on the next is expected to have the largest deteriorating effect on the image, when the screens are close to each other.

3. Simulation methodology

Several programs for simulating X-ray propagation are available such as *MCNP* (Briesmeister, 2000) and *GEANT4* (Allison *et al.*, 2006), capable of efficiently handling a large range of photon energies and materials. However, programs with the capability of handling the combination of both X-rays and visible photons are not readily available, and the effort of constructing dedicated simulation software was therefore deemed necessary. In the following we present a program for 'ray-tracing simulation for arrays of waveguiding scintillators' (*RAWS*), which handles both the local photon interaction with the nano-sized silicon walls and the long-range interaction of fluorescence and scattering events that extends hundreds of micrometers across the scintillator. It accurately finds the points where secondary emitted photons are generated and changes the propagation description to match the laws that govern the movements of these low-energy photons. The program also gives freedom to decide the properties of the initial X-ray photons by their positions and velocity vectors. By integrating photons and X-rays in the same code, the demands on memory are kept at a practical level. The code only keeps track of the geometry, which is repetitive, and the two-dimensional scoring plane.

The two-dimensional scoring plane in *RAWS* represents the CCD or CMOS in a camera. If the NA of the lens permits transmission of light at the angle of the incoming photon, the secondary emitted photons will be registered as intensity in an image. The coordinates of the intensity are determined by the final position of the photon. The output image consists of the number of registered photons integrated over each image pixel.

3.1. Modeling absorption events

This first part of the algorithm simulates the energy conversion from X-rays to excitons. The X-rays impinging on the scintillator are assumed to be unperturbed by the interfaces between the materials. They interact with the materials in the scintillator *via* absorption and scattering events. Throughout this paper, cross sections have been taken from the tabulations in NIST-XCOM (2004) unless noted.

A flow diagram of the absorption process is shown in Fig. 4. The most common interaction of the X-rays is with the core electrons of the atoms in the scintillator converting the X-ray photons into kinetic electrons and fluorescence photons with energies of the electron shell (Mengesha *et al.*, 1998). These particles in turn excite further electrons and photons until all the initial energy has been lost in exciton generation and lattice vibrations. The exciton relaxes when an electron finds an empty site in the lattice, and thus releases its energy in the form of a photon in the visible range. In some cases the initial

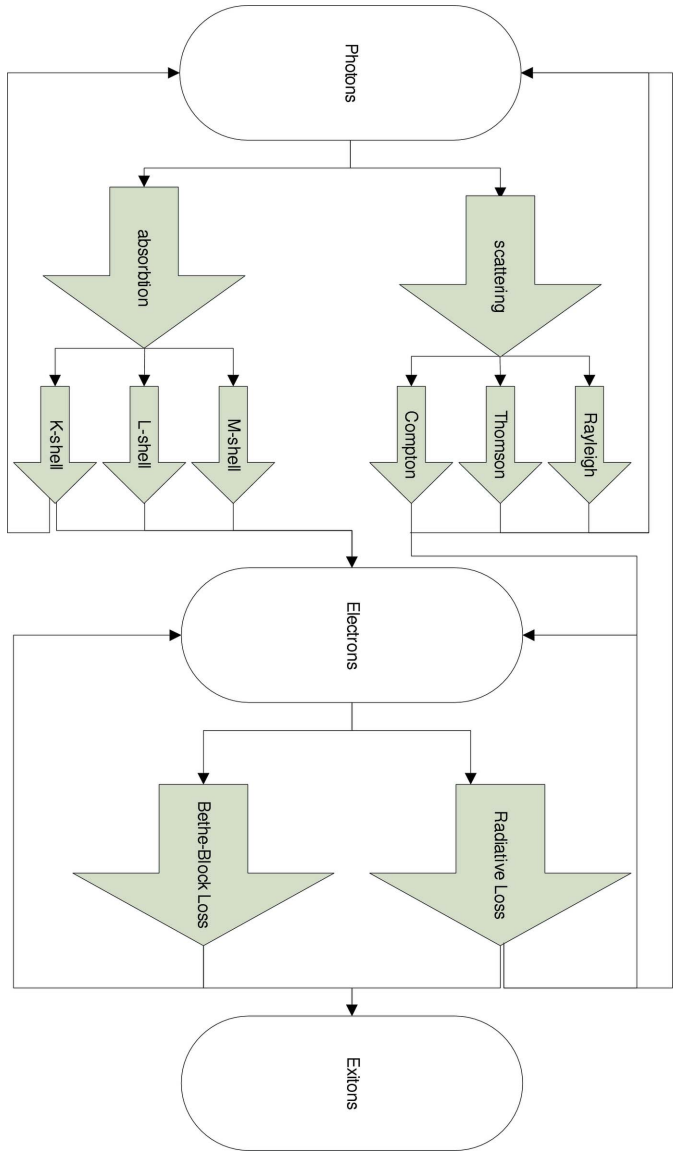

Figure 4
Flow chart of the parts in the *RAWS* algorithm representing interaction events influencing the X-rays and subsequently generated particles. Not shown are the secondary emitted photons that are generated at the sites of the excitons.

X-ray photon is not fully absorbed but only deflected either elastically without loss of energy in Thomson or Raleigh scattering processes or inelastically by Compton scattering where energy is lost according to the deflected angle (Poulsen & Neuefeind, 1995).

The *RAWS* algorithm uses the simplification of Bethe–Block in the version described by Joy and Lou (Jablonski *et al.*, 2006) to model the conversion of kinetic electrons to excitons. Their algorithm uses the energy of the particle to calculate an average path length between energy losses where electrons of higher energy move further between interacting with the crystal lattice.

To account for electron-generated radiation, the radiative cross section (NIST-ESTAR, 2003) is used to determine

probability for generation of kinetic photons or electrons after each translation of an electron.

3.2. Comparison with *MCNP*

The performance of the *RAWS* absorption model has been compared with the output from the commercially available simulation program *MCNP* (Briesmeister, 2000).

For this purpose the *RAWS* program is altered such that the absorbed energy is assigned to defined tally cells corresponding to the tally cells in *MCNP*. The *MCNP* code uses a tally construction separating the test volume into smaller voxels. The code presented in this paper uses an algorithm where each particle is accounted for separately, which gives the freedom to obtain information on a very detailed level, keeping track of how the absorbed energy originates from the different absorption mechanisms.

The structure chosen for the validation is a 100 µm-thick pillar made of CsI. The simulated beam is 150000 monochromatic photons with 50 keV energy. In Fig. 5, cross sections of absorbed charge are shown for the two algorithms. For the *MCNP* algorithm the charge is absorbed closer to the impact point of the photons than for the *RAWS* algorithm. The discrepancy is expected to be due to deviations in the energy-loss algorithms used for the two programs.

3.3. Ray-tracing of visible photons

The second part of the *RAWS* algorithm takes the input from the first part as a list of positions where an exciton is generated. It is assumed that the length scale of the excitons is negligible and that visible photons are emitted in the exact position of the excitons.

The visible photons or secondary emitted photons are generated with random direction vectors, and propagate through the structure according to Snell's law using non-complex refractive indices.

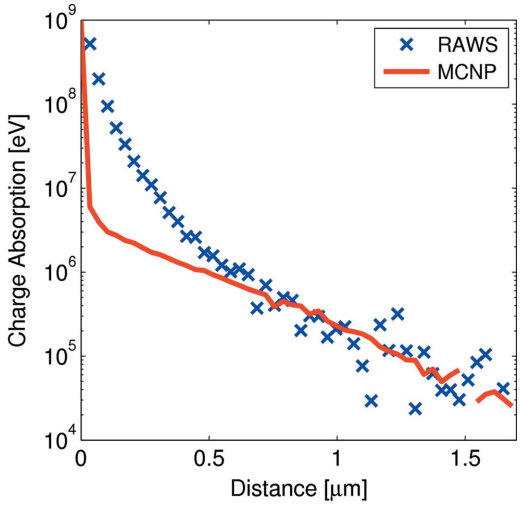

Figure 5
Comparison of the program *MCNP* (Briesmeister, 2000) and the *RAWS* algorithm presented in this article. The graph shows the amount of charge absorbed as a function of the distance from the X-ray impact.

The photons are propagated through the scintillating structure until they vanish at the sides or back of the structure or are absorbed in the SiO_2/silicon separating the pores. For the visible wavelengths silicon has an absorption length of 5 µm (Fox, 2001) which for simplicity is used for both silicon and silicon dioxide. For photons exiting on the front, the position of the photon is recorded on the camera screen if the numerical aperture of the lens allows the collection.

3.4. Implementation

The code has been written in *Matlab* on a Windows platform. Converted to a stand-alone executable program, a typical run time is 200 µs per X-ray photon.

4. Simulation of performance

The detector performance is simulated with regards to two aspects: spatial resolution and efficiency. The resolution R is evaluated from the PSF, and is found by simulating an infinite thin pencil beam averaged over the entire center pore including the Si/SiO_2 walls. The walls are assumed to be 500 nm thick for all simulations and made of a uniform material absorbing photons like silicon but having the refractive index of silicon dioxide. A lens has been added to the simulation *ad hoc* with perfect transmission, no aberrations and a NA of 0.57 which is thus capable of capturing all the photons exiting the pore.

In Fig. 6 the cross section from the two-dimensional scoring plane is shown for a simulated structured scintillator with a 1 µm pitch, 100 µm-deep pores and an energy of 50 keV. The structure of the scintillator is evident as peaks in the profile with an amplitude varying with the distance to the center in an Airy-like pattern. The discrete appearance implies that a conventional full width at half-maximum (FWHM) figure of merit is troublesome. As an alternative we define R_{90W} as the full width of the central fraction of the PSF containing 90% of the signal (see also Koch *et al.*, 1998).

Also shown in Fig. 6 is the simulated response of an unstructured 50 µm-thick CsI scintillator to 50 keV photons using a lens with a NA of 0.24. One of the main advantages of

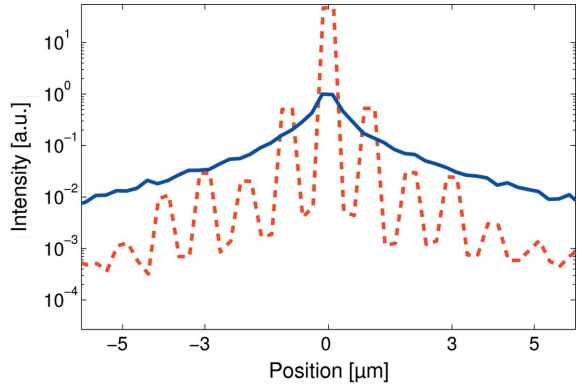

Figure 6
Part of the cross section of the scoring plane in *RAWS* simulating a structured scintillator with 1 µm pitch (dashed line). The solid line shows the cross section from an unstructured scintillator for comparison.

the structured scintillator concept is clearly demonstrated: the suppression of the tails by more than one order of magnitude.

The efficiency is defined as the ratio between inflicted dose and absorbed intensity in the central pore in the PSF image. In all simulations the dose on the scintillator is kept the same, but the incident beam is the size of the pitch, hence the flux is higher in scintillators with a small pitch.

In the characterization of the scintillator, three parameters are assumed to have the largest effect on the performance: pitch, height of the pores (scintillator thickness) and X-ray energy. Parametic studies have been made for the pitch at two characteristic energies, 50 and 90 keV, and for the energy at two characteristic pitches of 1 μm and 4 μm. The pore height was found to influence efficiency linearly and with negligible effect on the PSF, and the results will not be reported. In the following the pore height is kept constant at 100 μm.

4.1. Pitch

Varying the pitch shows a linear relationship between pitch size and PSF as seen in Fig. 7. This clearly demonstrates that the X-ray absorption is confined and the effect from scattering can be neglected. Owing to the decrease in active area, the efficiency decreases noticeably at a smaller pitch, making such a scintillator impractical unless the fabrication can be improved to give thinner walls. For a 0.75 μm pitch the active area is 11% and the low signal level leads to an increase in the R_{90W} measure.

The linear fit between the pitch of the pores and the resolution shows that multiple scattering is not prominent in determining the lower limit of resolution.

4.2. Resolution *versus* efficiency

In most applications both high resolution and high efficiency are required. From the simulations the efficiency of structured scintillators with different spatial resolution has been found. For unstructured scintillators, equation (3) has been used to find the efficiency as a function of resolution. The total efficiency is determined first by the X-ray absorption through the scintillator thickness and second by the NA through the size of the light cone that the lens collects from the total sphere of emitted light.

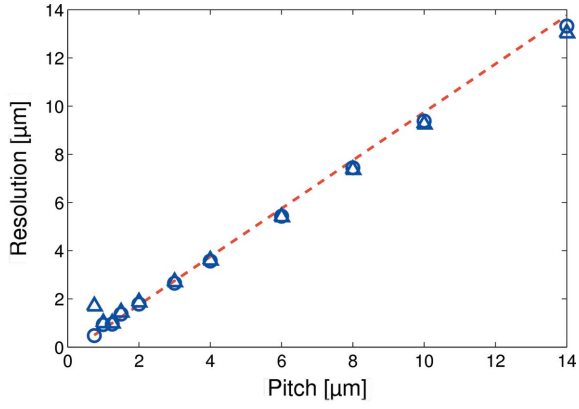

Figure 7
Spatial resolution *versus* the distance between pore centers in the structured scintillator. Dashed lines are FWHM measures for 90 keV and 50 keV which are not discernible, circles and triangles are R_{90W} measures for 50 keV and 90 keV, respectively.

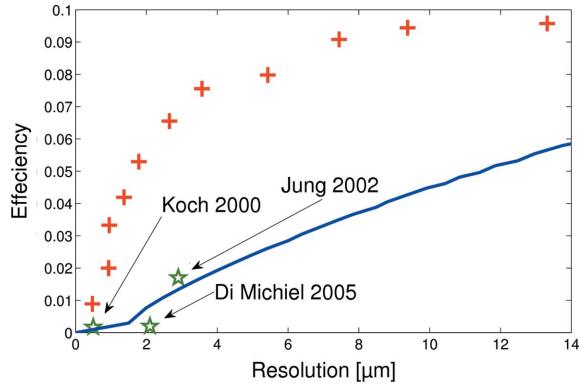

Figure 8
Efficiency *versus* resolution (R_{90W}) for an unstructured scintillator (solid line) and a structured scintillator (crosses). For comparison, experimentally found points are inserted (stars) from Jung *et al.* (2002), Di Michiel *et al.* (2005) and Koch *et al.* (2000).

Fig. 8 shows the efficiency *versus* resolution for both a structured scintillator and an unstructured scintillator. Additionally, experimental data points from the literature have been inserted. At high resolution the thickness of an unstructured scintillator prohibits high efficiency, whereas the efficiency of the structured scintillator stays at approximately the same level for all resolutions. The graph thus illustrates the resolution range that would benefit from the use of a structured scintillator. Two effects, however, are not considered in the graph. Firstly, the depth of the pores are assumed to be the same for all pitches, namely 100 μm. In practice, for a smaller pitch the depth is foreseen to decrease and for a larger pitch the pores could be made deeper. The second effect is from the numerical aperture of the lens; in the graph, z and NA have been adjusted to give the highest efficiency for a given resolution, which in principle means that the highest possible NA has been chosen which has been set to 0.4. While good 10× lenses can be found with a NA of 0.4, lenses of lower magnifications will have a lower NA and hence lower collection efficiency. The field of view for the 10× lenses of about 2–3 mm will for most users be unsatisfactory at resolutions above 4–6 μm.

The effect of the NA gives both detectors less efficiency for larger field of views but, where the unstructured detector needs the lens to focus, the structured scintillator could be positioned directly on a CCD with a matching pixel size, thereby maintaining efficiency. Presently CMOS chips with a pixel size of 2.5 μm are commercially available (Sony, 2007).

4.3. Energy

Simulations of the structured scintillator were performed while varying the energy from 32.7 keV to 200 keV. The resulting resolution as a function of energy is seen in Fig. 9. The increased scattering and fluorescence associated with higher energies are seen only to affect the 1 μm pitched screens, and only above 100 keV. The discrete nature of the

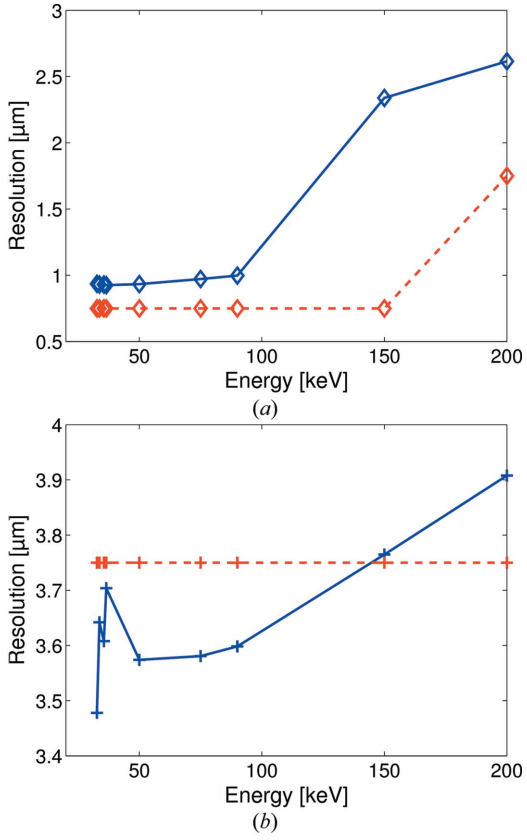

Figure 9
Resolution as a function of the X-ray energy for pitches of (*a*) 1 μm and (*b*) 4 μm. Solid lines are R_{90W} and dashed lines are FWHM measures.

fluorescence yield near the *K*-edges can be observed for the pitch of 4 μm as an increase in the resolution at energies just above the two *K*-edges at 33.2 keV and 36.0 keV, but the effect is negligible for practical purposes. The resolution found with a standard FWHM measure is seen to change less and only at higher energies compared with the R_{90W} measure that changes for smaller increases in photon energy.

4.4. Three-dimensional detector

In order to estimate whether the additional noise in a stacked detector would be detrimental to results, we simulated a tomography set-up with three screens placed after each other in the direction of the direct X-ray beam and placed 0.8 mm apart. The X-ray energy was 50 keV and the scintillating screens had a 2 μm pitch and 50 μm thickness; scattering events both in the forwards and backwards direction were followed. In Fig. 10(*a*) a test image is shown. It has small and large areas intermixed as well as a large dynamic range. These features resemble the characteristic image from a 3DXRD microscope. For comparison, the intensity of the third screen is shown in Figs. 10(*b*) and 10(*c*) with a linear and a logarithmic color map, respectively. As a result we found all scintillators to show the same signal-to-noise ratio. The multiple scattering is negligible for all practical purposes since the scattered X-rays average out in the image to a level that they do not interfere.

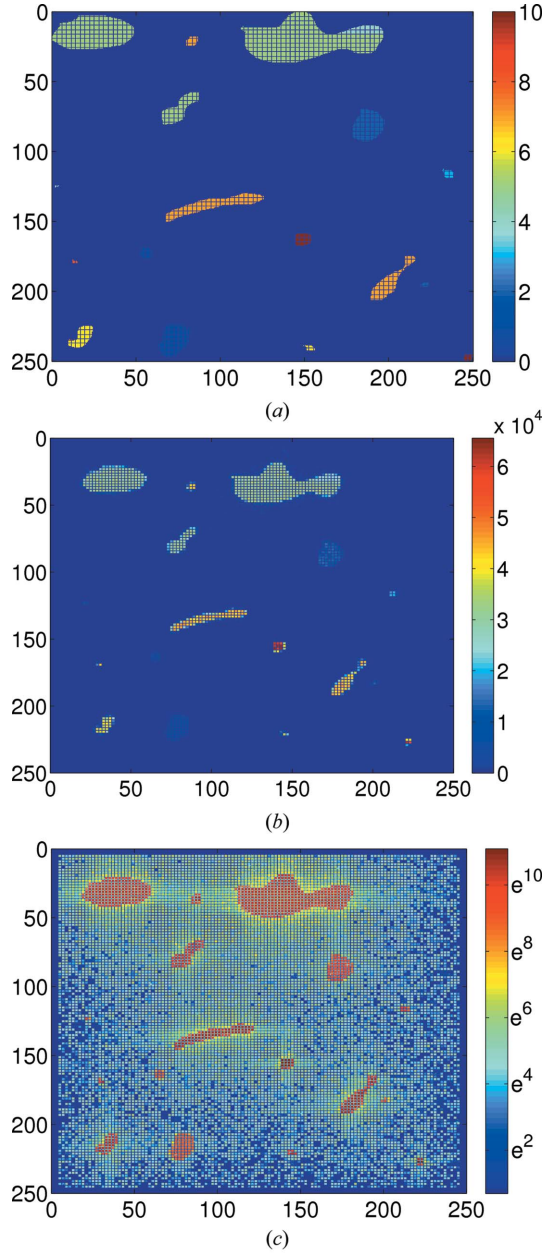

Figure 10
Simulation of the three-dimensional detector with three screens. Intensity map of the original image (*a*) and of the third screen (*b*, *c*). The scale in (*a*) and (*b*) is linear, and in (*c*) it is logarithmic. The color bars indicate intensity in arbitrary units. The background intensity level in the original image is zero.

5. Discussion and conclusions

The results presented clearly demonstrate the usefulness of the *RAWS* algorithm. The minor discrepancies evident in Fig. 5 between *MCNP* and *RAWS* are most likely attributable to simplifications in *RAWS*. However, the discrepancies suggest that cross sections and stopping mechanisms are underestimated for *RAWS* compared with *MCNP*. Since a more contained absorption would lead to less noise and better resolution, the conclusions made from this code hold to the extent that is presented in the following.

The simulations demonstrate that the spatial resolution is equal to the pitch of the structure, until sizes where the wall structure comprises a major part of the scintillator screen. This makes it worthwhile to pursue structured scintillator-based detectors with a resolution of 1 μm as well as exploring methods for achieving thinner walls. Since fabrication development is not finished, the exact dimensions of obtainable geometries are not known, but by using estimated geometries significant increases in efficiency can be expected for resolutions of less than 8 μm using the structured scintillator approach. The efficiency gain with respect to the unstructured scintillator design ranges from 5 to 15 for 8 μm to 1.5 μm, respectively. With the advent of photodetectors with a pixel size of a few micrometers, an approach where the structured scintillator is attached directly to the CMOS or CCD chip would, besides the increased efficiency, allow for a more compact design of the three-dimensional detector. Finally, the simulations show a resolution maintained for all energies up to at least 100 keV.

The set-up used here for the three-dimensional detector was generic in its nature; however, results indicate the feasibility of the principle. The increase of efficiency using multiple screens is inherent, while the implementation of super resolution demands further development of post-processing programs; however, the potential improvement is significant. Likewise, simultaneous images from multiple distances to the sample will give a decrease in the data acquisition time accordingly, which is of relevance in kinetic experiments. Compared with set-ups where a single detector is translated along the beam which is used for both diffraction studies and holographic techniques (Poulsen *et al.*, 2001; Cloetens *et al.*, 1999), the three-dimensional detector set-up thus eradicates unnecessary uncertainties from detector positions and from sample variations in time.

We would like to acknowledge Erik Nonbøl (Risø, DTU) and Mats Hjelm (Midsweden University) for an introduction to the *MCNP* code and useful discussions. Support from the Danish National Research Council, from the EU 6th Framework program 'TotalCryst' and from the ESRF are also gratefully acknowledged.

References

Allison, J. *et al.* (2006). *IEEE Trans. Nucl. Sci.* **53**, 270–278.
Badel, X. (2005). PhD thesis, Royal Institute of Technology (KTH), Stockholm, Sweden.
Badel, X., Galeckas, A., Linnros, J., Kleimann, P., Fröjdh, C. & Petersson, C. S. (2002). *Nucl. Instrum. Methods Phys. Res. A*, **487**, 129–135.
Banhart, J. (2008). *Advanced Tomographic Methods in Material Research and Engineering.* Oxford University Press.
Baruchel, J., Buffiere, J.-Y., Cloetens, P., Di Michiel, M., Ferrie, E., Ludwig, W., Maire, E. & Salvo, L. (2006). *Scr. Mater.* **55**, 41–46.
Bigler, E. & Polack, F. (1985). *Appl. Opt.* **24**, 994–997.
Briesmeister, J. (2000). *MCNP. A General Monte Carlo N-Particle Code.* Version 4C. Report LA-13709, Los Alamos National Laboratory, NM, USA.
Cloetens, P., Ludwig, W., Baruchel, J., van Dyck, D., van Landuyt, J., Guigay, J. P. & Schlenker, M. (1999). *Appl. Phys. Lett.* **75**, 2912.
Deckman, H. W., Dunsmuir, J. H. & Gruner, S. M. (1989). *J. Vac. Sci. Technol. B*, **7**, 1832–1835.
Di Michiel, M., Merino, J. M., Fernandez-Carreiras, D., Buslaps, T., Honkimäki, V., Falus, P., Martins, T. & Svensson, O. (2005). *Rev. Sci. Instrum.* **76**, 043702.
Fox, M. (2001). *Optical Properties of Solids.* Oxford University Press.
Holl, I., Lorenz, E. & Mageras, G. (1988). *IEEE Trans. Nucl. Sci.* **35**, 105.
Jablonski, A., Tanuma, S. & Powell, C. J. (2006). *Surf. Interface Anal.* **38**, 76–83.
Jung, H., Kim, H., Hong, S., Hong, J., Jeong, H., Ho Je, J., Kim, B. & Yoo, H. (2002). *IEEE Trans. Nucl. Sci.* **5**, 2262–2267.
Koch, A., Cloetens, P., Ludwig, W., Labiche, J. C. & Ferrand, B. (2000). *Proceedings of the 5th International Conference on Inorganic Scintillators and their Applications (SCINT99)*, pp. 157–166. Moscow State University, Moscow, Russia.
Koch, A., Raven, C., Spanne, P. & Snigirev, A. (1998). *J. Opt. Soc. Am. A*, **15**, 1940–1951.
Lehmann, V. (2002). *Electrochemistry of Silicon: Instrumentation, Science, Materials and Applications.* Weinheim: Wiley-VCH.
Lehmann, V. & Gruning, U. (1997). *Thin Solid Films*, **297**, 13–17.
Martin, T. & Koch, A. (2006). *J. Synchrotron Rad.* **13**, 180–194.
Mengesha, W., Taulbee, T., Rooney, B. & Valentine, J. (1998). *IEEE Trans. Nucl. Sci.* **45**, 456.
NIST-ESTAR (2003). *ESTAR*, http://physics.nist.gov/PhysRefData/Star/Text/ESTAR.html.
NIST-XCOM (2004). *XCOM: Photon Cross Sections Database*, http://physics.nist.gov/PhysRefData/Xcom/Text/XCOM.html.
Olsen, U. L. (2007). *Nucl. Instrum. Methods Phys. Res. A*, **576**, 52–55.
Park, S. C., Park, M. K. & Kang, M. G. (2003). *IEEE Signal Process. Mag.* **20**, 21–36.
Piemonte, C., Boscardin, M., Dalla Betta, G.-F., Ronchin, S. & Zorzi, N. (2005). *Nucl. Instrum. Methods Phys. Res. A*, **541**, 441–448.
Poulsen, H. (2004). *Three-Dimensional X-ray Diffraction Microscopy: Mapping Polycrystals and their Dynamics.* Berlin, New York: Springer.
Poulsen, H. & Neuefeind, J. (1995). *Nucl. Instrum. Methods Phys. Res. B*, **95**, 509–514.
Poulsen, H. F., Nielsen, S. F., Lauridsen, E. M., Schmidt, S., Suter, R. M., Lienert, U., Margulies, L., Lorentzen, T. & Juul Jensen, D. (2001). *J. Appl. Cryst.* **34**, 751–756.
Sony (2007). *Notes on IMX017CQE.* Technical Report, Sony Corporation, Japan.